JAMES | Journal of Advances in Modeling Earth Systems

RESEARCH ARTICLE
10.1029/2019MS001878

Application of the Cyclone Phase Space to Extratropical Transition in a Global Climate Model

Melanie Bieli[1], Adam H. Sobel[1,2], Suzana J. Camargo[2], Hiroyuki Murakami[3,4], and Gabriel A. Vecchi[5,6]

[1]Department of Applied Physics and Applied Mathematics, Columbia University, New York, NY, USA, [2]Lamont-Doherty Earth Observatory, Columbia University, Palisades, NY, USA, [3]Geophysical Fluid Dynamics Laboratory, National Oceanic and Atmospheric Administration, Princeton, NJ, USA, [4]Atmospheric and Oceanic Sciences Program, Princeton University, Princeton, NJ, USA, [5]Department of Geosciences, Princeton University, Princeton, NJ, USA, [6]Princeton Environmental Institute, Princeton University, Princeton, NJ, USA

Abstract The authors analyze the global statistics of tropical cyclones undergoing extratropical transition (ET) in the Forecast-oriented Low Ocean Resolution version of CM2.5 with Flux Adjustment (FLOR-FA). The cyclone phase space (CPS) is used to diagnose ET. A simulation of the recent historical climate is analyzed and compared with data from the Japanese 55-year Reanalysis (JRA-55), and then a simulation of late 21st century climate under Representative Concentration Pathway 4.5 is compared to the historical simulation. When CPS is applied to the FLOR-FA output in the historical simulation, the results diverge from those obtained from JRA-55 by having an unrealistic number of ET cases at low latitudes, due to the presence of strong local maxima in the upper-level geopotential. These features mislead CPS into detecting a cold core where one is not present. The misdiagnosis is largely corrected by replacing the maxima required by CPS with the 95th percentile values, smoothing the CPS trajectories in time, or both. Other climate models may contain grid-scale structures akin to those in FLOR-FA and, when used for CPS analysis, require solutions such as those discussed here. Comparisons of ET in the projected future climate with the historical climate show a number of changes that are robust to the details of the ET diagnosis, though few are statistically significant according to standard tests. Among them are an increase in the ET fraction and a reduction in the mean latitude at which ET occurs in the western North Pacific.

Plain Language Summary When tropical cyclones move into the midlatitudes, they change their physical structure and sometimes transform into extratropical cyclones. This process is called extratropical transition. One diagnostic tool for defining extratropical transition is the cyclone phase space. In this study, the authors apply the cyclone phase space to the tropical cyclones simulated by a global climate model. The output of this climate model has some features that misguide the cyclone phase space into diagnosing a cyclone as extratropical when in fact it is tropical. The authors examine various adjustments of the cyclone phase space that largely correct this misdiagnosis. They then study the changes in the global occurrence of extratropical transition between two 30-year time periods simulated by the climate model: a historical period from 1976 to 2005 and a future period from 2071 to 2100, whose simulation is based on a scenario of moderate increases in greenhouse gas emissions. In the western North Pacific, tropical cyclones are found to become more likely to undergo extratropical transition in the future climate. In general, though, the changes in global statistics of extratropical transition (e.g., where and how often it occurs) between the simulated future and historical climate are small.

Key Points:
- The cyclone phase space (CPS) is applied to diagnosing extratropical transition (ET) in FLOR-FA, a global climate model
- Strong local maxima in the FLOR-FA geopotential result in misdiagnosed ET cases, which can be corrected by a simple modification of the CPS
- Future changes in global statistics of ET are generally small but include an increase of the ET fraction in the western North Pacific

Supporting Information:
- Supporting Information S1

Correspondence to:
M. Bieli,
mb4036@columbia.edu

Citation:
Bieli, M., Sobel, A. H., Camargo, S. J., Murakami, H., & Vecchi, G. (2020). Application of the cyclone phase space to extratropical transition in a global climate model. *Journal of Advances in Modeling Earth Systems*, *12*, e2019MS001878. https://doi.org/10.1029/2019MS001878

Received 23 AUG 2019
Accepted 20 MAR 2020
Accepted article online 6 APR 2020

1. Introduction

Extratropical transition (ET) is the process in which some tropical cyclones (TCs) transform into extratropical cyclones, going from "symmetric" "warm core" circulation systems to "asymmetric" "cold core" systems, by interacting with midlatitude environments and weather systems (Evans et al., 2017; Jones et al., 2003). ET changes the physical structure of the cyclone and its associated hazards: The wind and precipitation fields expand in size and concentrate along frontal boundaries; the storm accelerates its forward motion and may produce large waves and swell (e.g., Bowyer & MacAfee, 2005; Evans et al., 2017; Jones et al., 2003; Matyas, 2013).

Climate change may alter the frequency, intensity, or geographical distribution of ET events. Several studies have used global climate models to study future changes in ET activity in the North Atlantic: Liu et al. (2017) find that storms undergoing ET account for most of the projected increase in TC frequency in the eastern North Atlantic. Haarsma et al. (2013) and Baatsen et al. (2015) show that these ET storms forming in the eastern Atlantic are responsible for a considerable increase in the frequency of hurricane-force winds affecting western Europe. Liu et al. (2018) explore the role of ET in projections of the rainfall associated with landfalling TCs in the eastern United States. In general, understanding the changing hazard requires knowing how both the storms' frequency and their physical properties (intensity, size, distribution of wind and rainfall, etc.) will change, and ET has been shown to alter storm properties in ways that are important for risk assessment (Loridan et al., 2014, 2015).

To the authors' knowledge, future projections of ET have only been studied in the Atlantic. This study takes a more general perspective and examines future simulations of ET activity in global ocean basins. TCs undergoing ET are identified by means of their trajectories through the cyclone phase space (CPS Hart, 2003), calculated from global climate model output. The CPS has become widely used and has been applied to diagnose ET in operational analysis and reanalysis data (e.g., Bieli et al., 2019a, 2019b; Hart, 2003; Kitabatake, 2011; Wood & Ritchie, 2014) as well as climate model output (Liu et al., 2017, 2018; Zarzycki et al., 2017). We use the Forecast-oriented Low Ocean Resolution version of CM2.5 with Flux Adjustment (FLOR-FA), which was developed at the Geophysical Fluid Dynamics Laboratory. FLOR-FA has been used to produce seasonal forecasts of TCs in the North Pacific and Atlantic (Murakami et al., 2016; Vecchi et al., 2014; Zhang et al., 2016), as well as to study ET and its rainfall hazard in the North Atlantic (Liu et al., 2017, 2018).

We begin this study by evaluating the global ET climatology simulated by FLOR-FA against that of the Japanese 55-year Reanalysis (JRA-55), for the historical climate. This evaluation reveals large differences, which can be traced back to structures in the simulated FLOR-FA fields that misguide the CPS diagnosis. The structures seem to be grid-scale ($50\,\text{km} \times 50\,\text{km}$) convective updrafts which manifest as strong local maxima in the geopotential height fields. Their presence invalidates the warm/cold core diagnosis in the CPS, which was developed on data sets that do not contain these structures.

Since the presence of TC-like vortices in simulations of global climate models was first noted in the 1970s (Camargo & Wing, 2016), increasing computational capacity and better numerical methods have led to substantial improvements in the models' abilities to simulate TCs. In recent years, horizontal grid spacings of 0.25–0.5° have become widely achievable. However, fully resolving the convection and clouds associated with TCs would require horizontal grid spacings of 0.1–1 km, so TCs are still under-resolved even in high-resolution climate models. Much modeling effort has been spent to find convection schemes and combinations of parameterized and resolved convection that give rise to realistic large-scale statistics of TC activity (e.g., TC frequency, intensity, geographic distribution, or interannual variability). Realism in these large-scale statistics is of the highest priority for studies on the relationship of TC activity to climate.

However, as this study shows, a realistic TC climatology does not preclude the possibility of unrealistic convective features in the simulated storms at the grid scale. In fact, such features are to be expected given that the numerical solutions of interest are far from convergence and in particular that the best TC properties seem to be achieved in some models when a non-negligible fraction of the convective mass flux occurs on the grid (e.g., Kim et al., 2018; Zhao et al., 2009). Until the resolution of global climate models becomes high enough to make convective parameterizations entirely unnecessary, such issues will remain. Algorithms such as the CPS that diagnose aspects of TC structure should—whenever possible—be designed to be applicable to as broad a range of climate data sets as possible. Since many of the models which currently provide the best simulations of large-scale TC statistics and their relationship to climate have horizontal grid spacings of tens of kilometers, and the potential for unrealistic grid-scale features as described above (and further below), it is desirable that such diagnostics, and CPS in particular, give reasonable results when applied to the output of such models.

In that spirit, we introduce a modification to the CPS that is designed to make the CPS diagnosis insensitive to the presence of strong local maxima in the input fields. The modified CPS and the original CPS method capture the same physical properties of TC structure and give similar results when no local maxima are present, but the modified CPS has the advantage of also producing physically sensible results in cases where those maxima are present. We compare the effect of this new modification on the historical ET climatology to the effect of a temporal smoothing of the CPS parameters (a commonly applied modification to the CPS)

and to the combined effect of the new modification and the smoothing. The sensitivity of the results to these modifications to the CPS (which we will sometimes refer to as "CPS experiments") is also explored in the subsequent analysis of future changes in global ET activity.

2. Data and Methods

2.1. FLOR-FA Climate Model

The model output analyzed in this study was produced by the Forecast-oriented Low Ocean Resolution (FLOR) version of CM2.5, developed at the Geophysical Fluid Dynamics Laboratory (Jia et al., 2015; Vecchi et al., 2014). FLOR combines the high-resolution (approximately 50 km × 50 km horizontal grid spacing) land and atmosphere components of the fully coupled CM2.5 (Delworth et al., 2012) with ocean and sea ice components derived from its lower-resolution (approximately 1° × 1° horizontal grid spacing) predecessor model, CM2.1 (Delworth et al., 2006). We use a version of FLOR called FLOR Flux-Adjusted (FLOR-FA), in which momentum, freshwater, and enthalpy fluxes between the atmosphere and ocean are corrected with climatological adjustments. The implementation of the flux adjustment is described in Vecchi et al. (2014). FLOR uses a finite volume dynamical core on a cubed-sphere grid (Putman & Lin, 2007) and a Relaxed Arakawa-Schubert convection scheme (Moorthi & Suarez, 1992).

The FLOR model has skill in the simulation and seasonal prediction of TCs (Murakami et al., 2016; Vecchi et al., 2014) and extratropical cyclones (Yang et al., 2015) and—used as a basis for a hybrid statistical-dynamical model—in the prediction of North Pacific landfalling TCs a few months in advance (Zhang et al., 2017). Liu et al. (2017) use FLOR to study ET in the North Atlantic and show that the ET climatology simulated by FLOR broadly agrees with those derived from reanalysis data sets. FLOR's higher-resolution successor model (HiFLOR, Murakami et al., 2015) has been used to study rainfall associated with North Atlantic ET events (Liu et al., 2018) as well as the potential for seasonal prediction of these events (Liu et al., 2018).

Here, we analyze a five-member ensemble of historical (1976–2005) and future (2071–2100) climate simulated by the FLOR-FA model, output at a horizontal resolution of 50 km × 50 km. The end years of these two 30-year time periods match those of the 1986–2005 and 2081–2100 time periods used for analyzing the historical climate and projected future changes in the IPCC's Fifth Assessment Report (Stocker et al., 2013). The five ensemble members are obtained by perturbing initial conditions in simulations spanning the time period 1861 to 2100. In these simulations, the historical anthropogenic forcing, volcanic radiative forcing, and aerosols are prescribed up to 2005, and the period 2006–2100 is forced by the RCP4.5 scenario, a "medium mitigation scenario" in which total radiative forcing is stabilized shortly after 2100, at roughly 4.5 W/m^2 above preindustrial, globally averaged (Clarke et al., 2007; Thomson et al., 2011). Detailed descriptions of the ensemble experiments in FLOR-FA are available in Murakami et al. (2017) and Murakami et al. (2015).

2.2. JRA-55 Reanalysis

The reanalysis data set used in this study is the six-hourly JRA-55 (Kobayashi et al., 2015) at a horizontal resolution of 1.25° × 1.25°. In its four-dimensional variational data assimilation, JRA-55 incorporates artificial wind retrievals in the vicinity of TCs. These retrievals are generated by a combination of three wind models, which reconstruct 3-D wind profile data at certain locations around the storm center, using TC information from best track data (Fiorino, 2002). In the assimilation process, the wind profiles are treated like regular observations from dropwindsondes (Ebita et al., 2011; Hatsushika et al., 2006). Comparing six reanalysis data sets, Murakami (2014) finds that JRA-55 has the highest TC detection rate, the lowest false alarm rate, and the most skill in simulating the spatial and temporal distribution of TC occurrence. Two of the six reanalysis data sets analyzed in Murakami (2014) were also examined by Zarzycki et al. (2017), who found similar numbers for the TC hit rates of these two reanalyses despite using a different tracking algorithm. Bieli et al. (2019b) show that the classification of TCs into "ET storms" (storms that undergo ET) and "non-ET storms" (storms that do not undergo ET) obtained from JRA-55 (using the CPS) agrees better with the best track classification than that obtained from the ECMWF interim reanalysis.

We use JRA-55 data from 1979 to 2005 to generate a historical ET climatology that is compared with the 1979–2005 ET climatology obtained from FLOR-FA. The quality of reanalysis products increased markedly in 1979 when vast quantities of satellite sounding data started to be assimilated (e.g., Bromwich et al., 2007).

Table 1
Summary of the Algorithms to Compute the Five Sets of CPS Parameters Used in This Study

	JRA-55	FLOR-FA	FLOR-FA, p95	FLOR-FA, sm	FLOR-FA, p95 + sm
$-V_T$ parameters	Equation (1)	Equation (1)	Equation (1) with Z_{max} replaced by Z_{p95}	Equation (1)	Equation (1) with Z_{max} replaced by Z_{p95}
B parameter	Equation (2)	Equation (2)	Equation (2)	Equation (2)	Equation (2)
Smoothing	No	No	No	Yes	Yes

Note. The smoothing is a 24-hr running mean along the time series of CPS parameters along each TC track. Z_{max} is the maximum value of geopotential height within 500-km radius around the storm center, and Z_{p95} is the 95th percentile of geopotential height within that domain (see section 2.3 for details).

We therefore use the time period 1979–2005, the overlap of the satellite era (1979–present) with the period of FLOR-FA historical data (1976–2005), for comparisons between JRA-55 and FLOR-FA.

2.3. CPS and Identification of ET Storms

The TCs in FLOR-FA are tracked from six-hourly model output using the tracking algorithm developed in Harris et al. (2016), with parameter settings as in Murakami et al. (2015). This tracking scheme mainly uses sea level pressure, near-surface winds, and the temperature anomaly averaged between 300 and 500 hPa to identify and track TCs. The thermal characteristics of these TCs are examined using the CPS (Hart, 2003), which consists of three parameters that measure the 900- to 600-hPa geopotential thickness asymmetry across the storm (parameter B), the upper-level (600–300 hPa) thermal wind (parameter $-V_T^U$), and the lower-level (900–600 hPa) thermal wind (parameter $-V_T^L$). All three parameters are computed from geopotential height fields within a radius of 500 km around the center of the cyclone, defined by the storm center position in the best tracks when performing CPS analysis in JRA-55, and by the position of the tracked cyclone when performing CPS analysis in FLOR-FA. Detailed descriptions can be found in Hart (2003) and Evans and Hart (2003).

Following Liu et al. (2017), who use FLOR to examine ET in the North Atlantic, we use a simplified method to calculate the CPS parameters, since six-hourly geopotential height fields are only output at three pressure levels. For consistency, the same method is also used for the computation of the CPS parameters in JRA-55, despite the availability of output at all pressure levels needed to compute the "full" CPS. In this simplified method, the thermal wind parameters are computed from geopotential height at two pressure levels (300 and 500 hPa for $-V_T^U$ and 500 and 850 hPa for $-V_T^L$) instead of the linear regression through multiple levels used in the original method by Hart (2003):

$$-\mathrm{V}_T^U = \frac{\Delta Z_{300} - \Delta Z_{500}}{\ln 300 - \ln 500},$$
$$-\mathrm{V}_T^L = \frac{\Delta Z_{500} - \Delta Z_{850}}{\ln 500 - \ln 850}. \quad (1)$$

$\Delta Z = Z_{max} - Z_{min}$ is the difference between maximum and minimum geopotential height within 500 km of the storm's center, at the pressure level (in hPa) indicated by the subscript. This difference is used as a discrete approximation to the magnitude of the geopotential height gradient, which in turn is proportional to the magnitude of the geostrophic wind; hence, $-V_T^U$ and $-V_T^L$ are essentially proportional to an approximated thermal wind magnitude (Hart, 2003). The sign is chosen such that positive values of $-V_T^U$ and $-V_T^L$ correspond to weakening geostrophic winds with height and thus to the presence of a warm core in that layer.

The B parameter is calculated as the storm-motion-relative 850- to 500-hPa thickness gradient across the cyclone:

$$B = h\left(\overline{Z_{500\mathrm{hPa}} - Z_{850\mathrm{hPa}}}\Big|_{\mathrm{R}} - \overline{Z_{500\mathrm{hPa}} - Z_{850\mathrm{hPa}}}\Big|_{\mathrm{L}}\right), \quad (2)$$

where Z is geopotential height, R indicates right relative to the storm motion, L indicates left relative to the storm motion, and the overbar indicates the areal mean over a semicircle of radius 500 km. The hemispheric parameter h is 1 for the Northern Hemisphere and −1 for the Southern Hemisphere.

In addition to the basic definitions given in equations (1) and (2), we generate three more sets of CPS parameters from FLOR-FA data by modifying their calculation in the following ways: The first modification, which

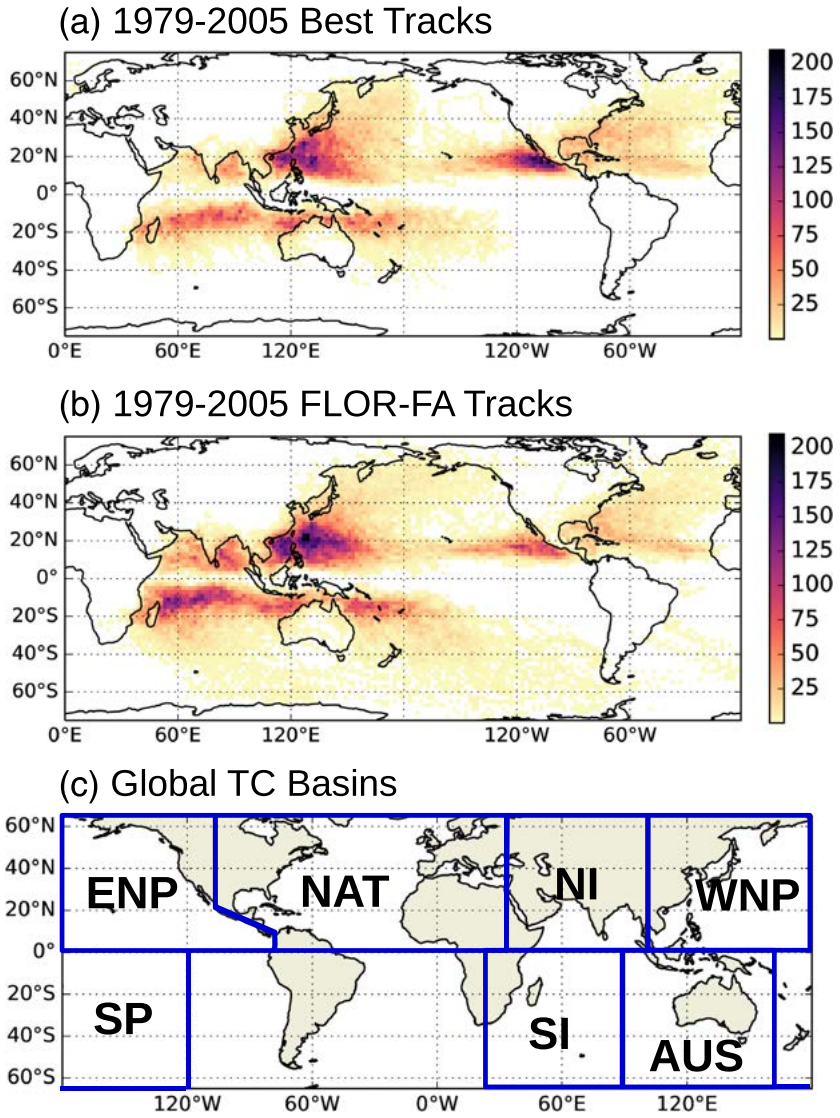

Figure 1. Comparison of TC track densities: (a) global best tracks ($n = 2{,}292$) and (b) tracks of TCs in one FLOR-FA ensemble member ($n = 2{,}497$), from the Harris et al. (2016) tracking algorithm. The plots show the sums of all track points falling into each $2° \times 2°$ grid box over the time period 1979–2005, which is the period used when comparing FLOR-FA and JRA-55 (sections 3.1 and 3.2). The future projections of ET activity (section 3.3) are based on FLOR-FA tracks from 1976 to 2005 and from 2071 to 2100. (c) Global TC basins: North Atlantic (NAT), western North Pacific (WNP), eastern North Pacific (ENP), North Indian Ocean (NI), South Indian Ocean (SI), Australian region (AUS), and South Pacific (SP).

we call "p95," is the use of Z_{p95}, the 95th percentile of Z, instead of the maximum value of Z within 500 km around the storm center. This changes the definition of ΔZ in equation (1) to $\Delta Z = Z_{p95} - Z_{\min}$. The second modification is a smoothing of all the CPS parameters (abbreviated "sm") using a 24-hr running mean along the six-hourly time steps of the TC tracks. A further set of parameters, "p95 + sm," combines the two previous modifications by applying the temporal smoothing to time series of CPS parameters that are calculated using the p95 method. Table 1 summarizes the four algorithms used to compute CPS parameters in FLOR-FA.

In JRA-55, the CPS is calculated using global best track data from 1979 to 2005, with the simplified method given by equations (1) and (2). The best track data sets are from the National Hurricane Center in the North Atlantic and in the eastern North Pacific, from the Japan Meteorological Agency in the western North Pacific, and from the Joint Typhoon Warning Center in the North Indian Ocean and in the Southern

Hemisphere basins. Figure 1 gives an overview of the global TC tracks used in this study, together with the boundaries of the ocean basins.

Following Bieli et al. (2019a, 2019b), ET is defined as follows: ET onset is the first time a TC is either asymmetric ($B > 11$) or has a cold core ($-V_T^L < 0$ and $-V_T^U < 0$), and ET completion is when the second criterion is met. Bieli et al. (2019a, 2019b) also require a minimum wind speed of 34 kt (≈17.5 m/s; tropical storm intensity) for ET onset in order to prevent weak, thermally asymmetric tropical depression-like systems or monsoonal troughs from being incorrectly diagnosed as beginning ET events. Based on the objectively determined relationship between tropical storm intensity and model resolution given in Walsh et al. (2007), the minimum wind speed for the onset of ET in FLOR-FA is set to 16.5 m/s, as this is approximately the equivalent intensity of a tropical storm in a model with 50-km horizontal resolution.

3. Results

3.1. Distributions of CPS Parameters in JRA-55 and FLOR-FA

We start by comparing the distributions of the CPS parameters along tracks of storms obtained from FLOR-FA with those from JRA-55, for the period 1979–2005. Figures 2a and 2b show the joint distributions of the B and $-V_T^L$ parameters. In both data sets, the peak frequency in the B versus $-V_T^L$ cross section of the CPS corresponds to storms with high thermal symmetry ($B \approx 0$) and a low-level warm core ($-V_T^L > 0$). The strongest thermal asymmetries tend to go along with the strongest cold cores. The $-V_T^U$ versus $-V_T^L$ distributions (Figures 3a and 3b) show that in JRA-55, deep warm cores ($-V_T^U > 0$ and $-V_T^L > 0$) are the most common vortex structures, and the upper- and lower-level thermal winds are positively correlated. In FLOR-FA, the distribution bulges into the lower right quadrant, indicating a large proportion of vortices with upper-level cold cores and intense low-level warm cores. On average, TCs in FLOR-FA have warmer lower-level cores but colder upper-level cores than the TCs in JRA-55.

Figures 2 and 3 also show the distributions resulting from the modifications in the calculation and/or post-processing of the CPS parameters described in section 2.3: Using the 95th percentile instead of the maximum value of geopotential height to compute the thermal wind parameters (p95) shifts the peak $-V_T^U$ versus $-V_T^L$ frequencies into the deep warm core (upper right) quadrant (Figures 3c and 3f), where they are also located in the JRA-55 distribution (Figure 3a), and where one would expect them to be located given the tropical nature of the cyclones. Applying a 24-hr running-mean smoothing (sm) produces distributions that are narrower than those of the unmodified CPS parameters. This effect can be seen in both the $-V_T^U$ versus $-V_T^L$ and B versus $-V_T^L$ diagrams. However, in contrast to the p95 experiment, the peak $-V_T^U$ versus $-V_T^L$ frequencies remain in the lower right quadrant (Figure 3d). The combined experiment (p95 + sm) shows both the narrowing effect and the shift to a maximum in the deep warm core quadrant (Figures 2e and 3e).

A part of the variation between the CPS distributions of JRA-55 and FLOR-FA may be due to the differences in the underlying TC tracks (Figure 1). Especially in the Southern Hemisphere, the FLOR-FA tracks extend farther poleward than the best tracks. As a crude test of how the track length affects the CPS distributions, the FLOR-FA tracks were cut off poleward of fixed, basin-specific threshold latitudes, defined as the 95th percentiles of the distributions of best track end point latitudes. The CPS distributions of the shortened FLOR-FA tracks (not shown) are very similar to those of the original FLOR-FA tracks described above, suggesting that the differences do not result primarily from FLOR-FA storms reaching higher latitudes than the best track storms but from differences that occur within a latitude range passed by storms from both sets of tracks.

While temporal smoothing is a frequently used method to remove short-term noise in the CPS trajectories (e.g., Hart, 2003; Liu et al., 2017; Zarzycki et al., 2017), the p95 experiment is designed to address a specific characteristic of FLOR-FA output that results in faulty thermal wind ($-V_T^U$ and $-V_T^L$) parameters and therefore in an incorrect diagnosis of a cyclone's warm/cold core structure. As described in section 2.3, the computation of the CPS parameters is based on six-hourly fields of geopotential height within a circle of radius 500 km around the storm center. In FLOR-FA, these input fields sometimes feature strong local maxima such as those shown in Figure 4b. The spots of increased geopotential height are confined to a few grid points and typically last on the order of 6 hr or less. We expect that their presence is the result of vigorous grid-scale updrafts, whose occurrence in the model is controlled in part by how strongly the divergent component of the horizontal flow is damped (e.g., Anber et al., 2018; Zhao & Held, 2012). This so-called

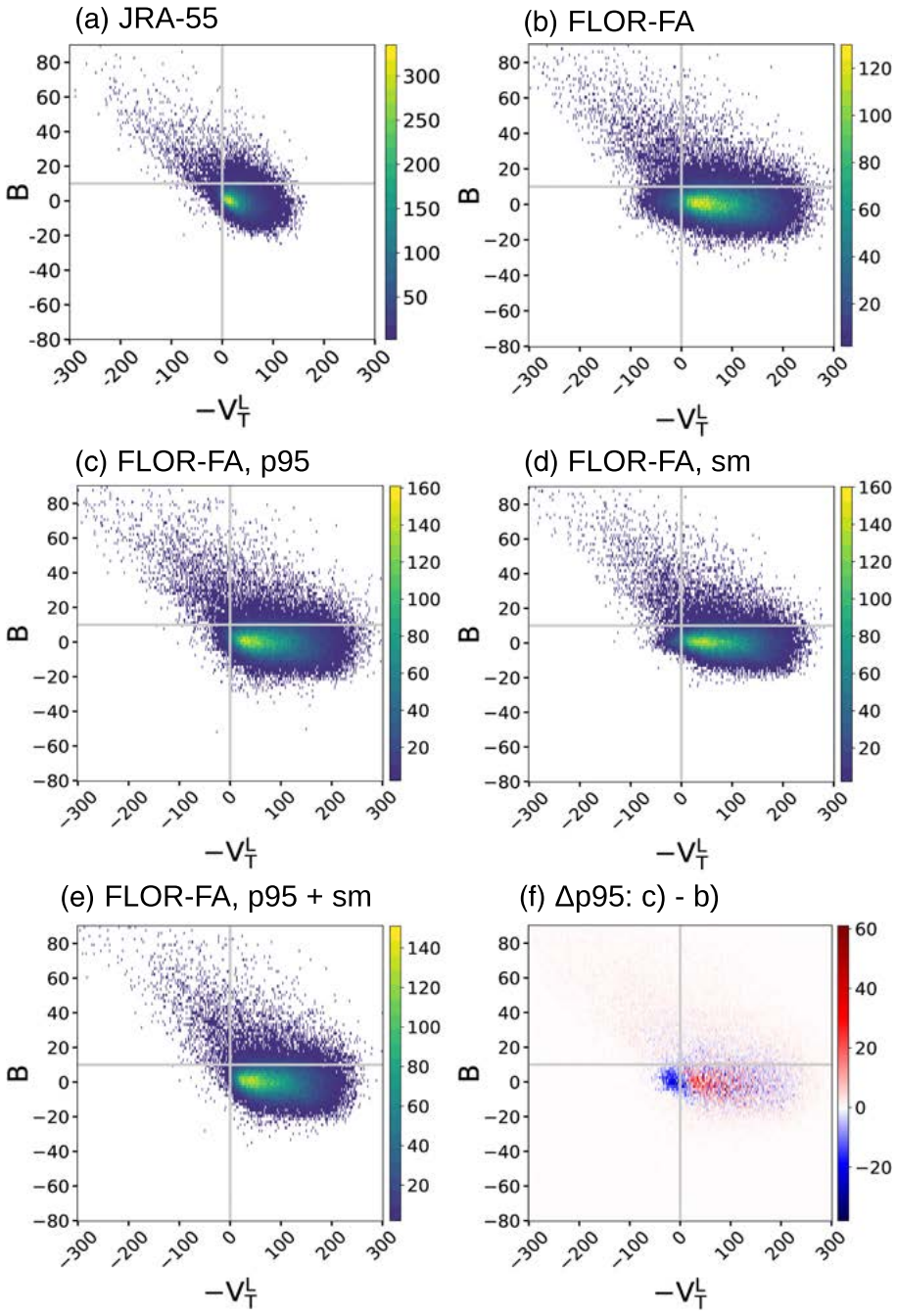

Figure 2. Joint distributions of the CPS parameters B and $-V_T^L$, derived from (a) JRA-55 and (b–e) FLOR-FA. In p95, $-V_T^L$ is computed using the 95th percentile of the geopotential height distribution, and in sm, a temporal smoothing is applied (see section 2.3 for a more detailed description of these modifications). The distribution in (f) is the difference between (c) and (b), that is, the difference between the FLOR-FA p95 distribution and the unmodified FLOR-FA distribution. The JRA-55 parameters shown in (a) are unmodified (no p95 or smoothing). All distributions are based on TCs in the period 1979–2005 (2,497 TCs from the first ensemble member in FLOR-FA and 2,292 TCs from global best track data in JRA-55).

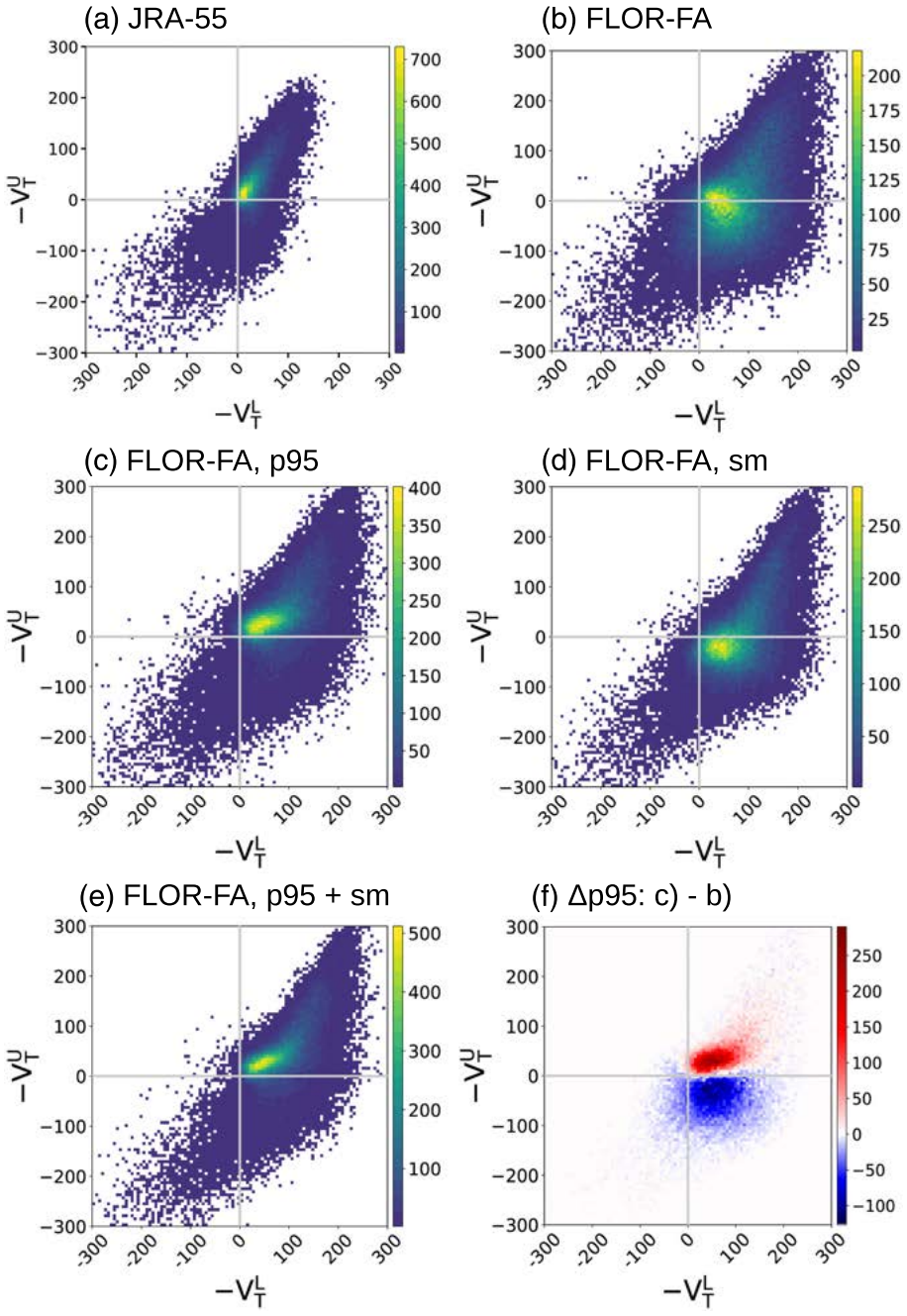

Figure 3. Joint distributions of the CPS parameters $-V_T^U$ and $-V_T^L$, derived from (a) JRA-55 and (b–e) FLOR-FA. In p95, $-V_T^U$ and $-V_T^L$ are computed using the 95th percentile of the geopotential height distribution, and in sm, a temporal smoothing is applied (see section 2.3 for a more detailed description of these modifications). The distribution in (f) is the difference between (c) and (b), that is, the difference between the FLOR-FA p95 distribution and the unmodified FLOR-FA distribution. The JRA-55 parameters shown in (a) are unmodified (no p95 or smoothing). All distributions are based on TCs in the period 1979–2005 (2,497 TCs from the first ensemble member in FLOR-FA and 2,292 TCs from global best track data in JRA-55).

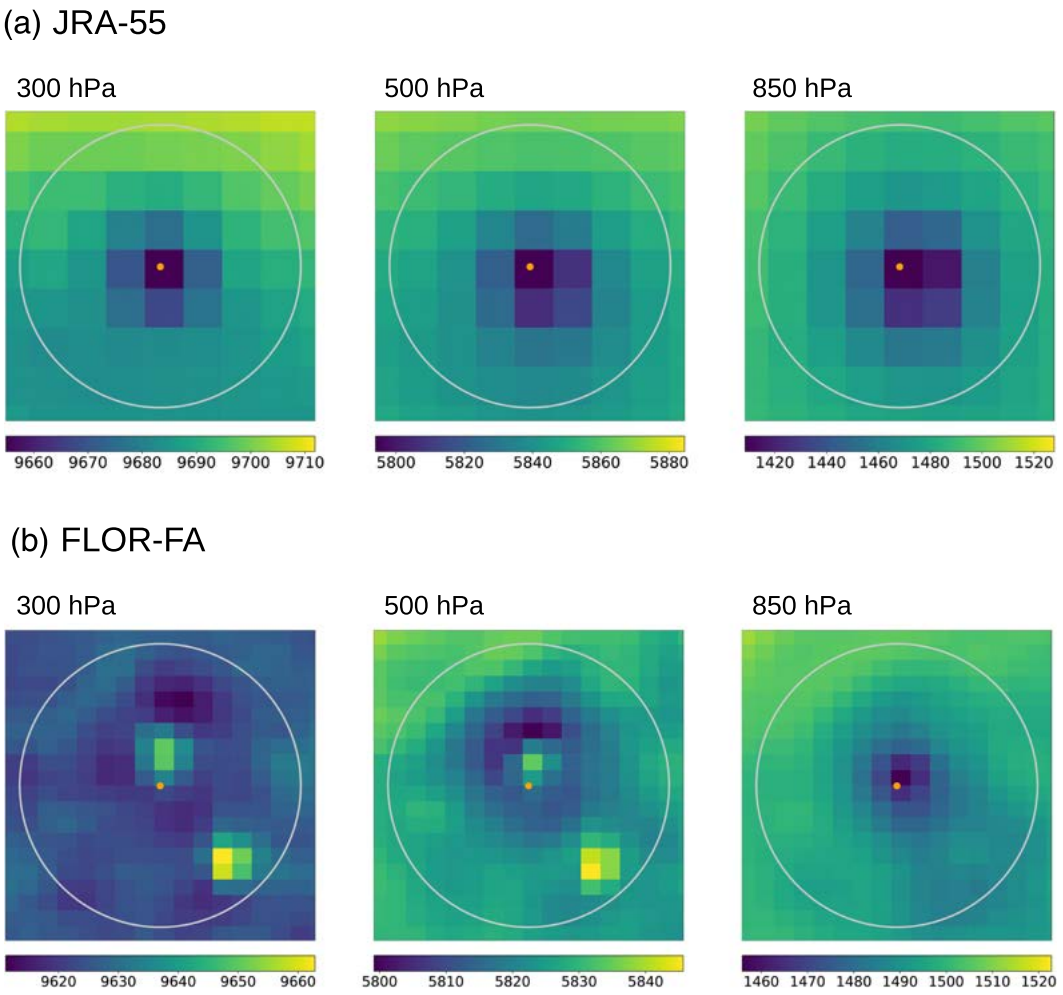

Figure 4. Storm-centered geopotential height fields in (a) JRA-55 and (b) FLOR-FA (first ensemble member). The fields are six-hourly snapshots taken at 300, 500, and 850 hPa. The gray circle has a radius of 500 km from the storm center, which is marked as an orange dot. Date, time, storm location, and intensity are (a) 14 April 1979, 06 UTC, 8.2°N/130.5°E, 28.3 m/s, and (b) 11 January 1976, 06 UTC, 6.2°N/60.5°E, 18.0 m/s. The snapshots were chosen for illustrative purposes, to give an example of the grid-scale structures observed in FLOR-FA (present here at the 300- and 500-hPa levels), and the absence of such structures in JRA-55.

divergence damping is used in numerical models to prevent the buildup of shortwave energy. It is implemented as a diffusion term that is added to the discretized version of the horizontal momentum equation. The weaker the damping, the noisier the simulated fields, and the stronger and narrower the resulting convective updrafts (Anber et al., 2018).

Probability distributions of the numbers of strong local maxima (Figure 5) were obtained by applying a maximum filter to six-hourly storm-centered geopotential height fields (500 km × 500 km) along all TC tracks from 1979 to 2005. To be considered "strong," a local maximum has to exceed the 95th percentile of the field under consideration. Figure 5 shows that in FLOR-FA, about two thirds of the 300-hPa fields and a fourth of the 500-hPa fields contain at least one strong local maximum. There is almost no difference in these distributions between the five ensemble members (not shown). In contrast, strong local maxima are nonexistent in JRA-55.

The computation of the $-V_T^U$ and $-V_T^L$ parameters (equation 1) uses the largest value of geopotential height within 500 km of the diagnosed storm center and is thus sensitive to grid-scale updrafts that generate a global maximum of geopotential height within that domain. The fact that these updrafts are most prevalent at the 300-hPa level (Figure 5b) explains the frequent occurrence of cyclones diagnosed as having an upper-level cold core (Figure 3b): If grid-scale convection causes an artificially high value of ΔZ at 300 hPa,

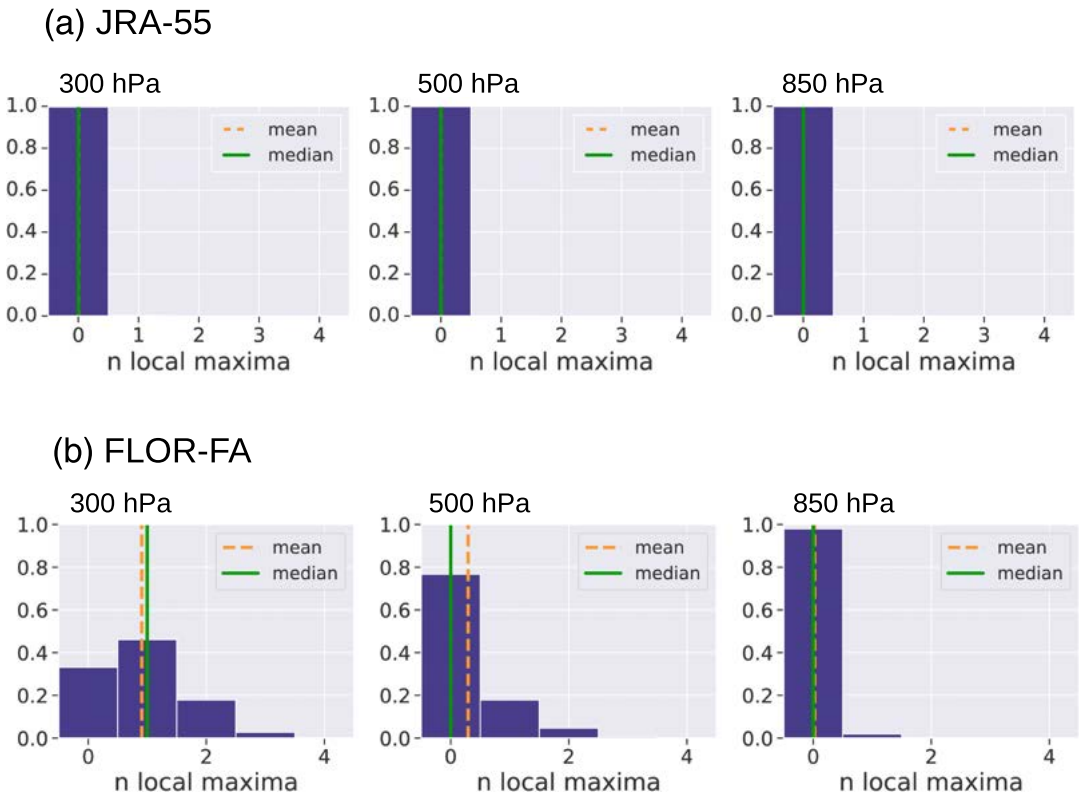

Figure 5. Histograms of the number of strong local maxima in six-hourly geopotential height fields within 500 km of the storm center in (a) JRA-55 and (b) FLOR-FA. A "strong" local maximum is defined here as one that exceeds the 95th percentile of the geopotential height field under consideration. Points on the boundary of the domain are excluded. The histograms show the data from all TCs in the period 1979–2005, amounting to a total of 73,981 fields in JRA-55 and 475,412 fields from the five FLOR-FA ensemble members.

the nominator in equation (1) is positive, which results in a negative (cold core) value of $-V_T^U$. The thermal wind parameters are supposed to measure the vertical profile of the geopotential height gradient between the cyclone's core and its outer region. The local maxima, which were not present in the reanalysis and forecast data on which the CPS was developed by Hart (2003), derail the computation of these gradients and mislead the CPS diagnosis. The "full" CPS method, in which the thermal wind parameters are calculated from a linear regression through geopotential height values at seven pressure levels, may be slightly more robust to the presence of outliers than the simplified CPS, in which each parameter is computed from only two values. However, outliers are given disproportionate weight in ordinary least squares regression and would likely still exert a strong influence on the resulting slope of the regression line. In addition, applying the full CPS would not address the underlying problem, that is, the clearly unphysical geopotential height gradients caused by the local maxima.

The p95 method attempts to correct the diagnostic failures described above by making the thermal wind parameters insensitive to (positive) extreme values. As shown in Figure 3c, replacing the maximum with the 95th percentile indeed reduces the presence of cold core vortices in the data set. Given the 50-km resolution of FLOR-FA and the typical size of the convective updrafts (approximately 6–8 grid points), ignoring the highest 5% of geopotential height values generally amounts to removing an area the size of about 1–2 local maxima. Note that p95 would not preclude a misdiagnosis due to a spurious global minimum resulting from a strong downdraft. While we did not find any such cases in FLOR-FA, a straightforward solution to this problem would be to replace the minimum geopotential height value with the 5th percentile.

Finally, an alternative solution to p95 would be a spatial smoothing of the geopotential height fields used to compute the CPS parameters. Though we considered this option, we preferred to address the problem at the level of the CPS algorithm itself rather than at the level of its input. In contrast to a spatial smoothing, the p95 method directly improves the ability of the CPS method to deal with noisy fields, and it has the advantages of being simpler, more general, and data set independent (e.g., the p95 method can be used whether or not

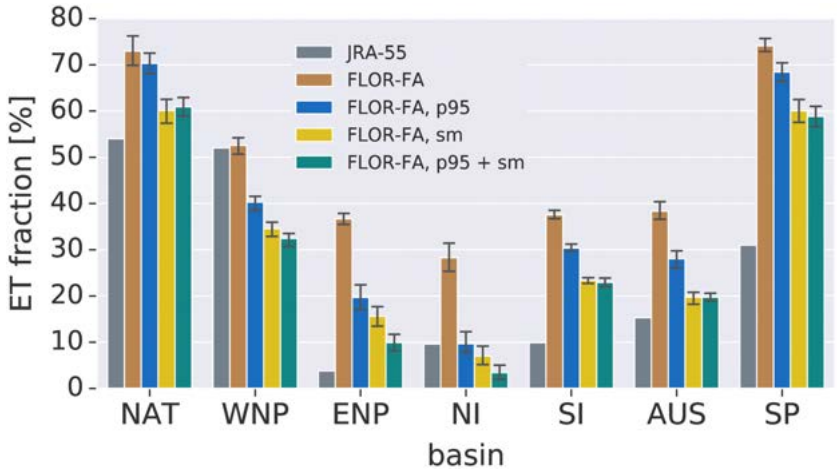

Figure 6. Global ET fractions (1979–2005) from JRA-55 and FLOR-FA, in the North Atlantic (NAT), western North Pacific (WNP), eastern North Pacific (ENP), North Indian Ocean (NI), South Indian Ocean (SI), Australian region (AUS), and South Pacific (SP). The error bars in FLOR-FA show the 95% confidence interval estimated from five ensemble members.

the underlying fields are noisy—in the absence of noise, the result will be similar to what the original CPS method would produce).

3.2. Historical ET Activity: Sensitivity to CPS Algorithm

Differences in the distributions of the CPS parameters may translate into differences in the statistics of ET occurrence. Figure 6 shows the fractions of storms undergoing ET in each basin, according to the CPS-based definition of ET given in section 2.3. The ET fractions in FLOR-FA are generally higher than those in JRA-55, but they have a similar overall pattern with the highest fractions in the North Atlantic, South Pacific, and western North Pacific basins and the lowest fraction in the North Indian Ocean. As in the previous section, comparing JRA-55 and FLOR-FA fractions is not an apples-to-apples comparison due to the differences in the underlying tracks. While shortening the FLOR-FA tracks does not change the characteristics of the CPS distributions (section 3.1), it has some effect on the resulting ET fractions: In the Southern Hemisphere basins, the ET fractions of the shortened tracks are about 5–10 percentage points below those of the original tracks. In the Northern Hemisphere basins, however, the ET fractions remain nearly unchanged (Figure S1 in the supporting information).

Within the four FLOR-FA experiments, both the p95 modification and (to a greater extent) the smoothing decrease the ET fractions compared to those from the unmodified parameters. This is an expected result as both p95 and the smoothing alleviate the effects of spurious diagnoses of cold cores as described in the previous section and thereby lower the probability of false positive ET events. The lowest ET fractions result from combining p95 and the smoothing. The fraction of 60% for the smoothed experiment in the North Atlantic closely matches the result by Liu et al. (2017), who also applied a 24-hr running mean to the CPS parameters and obtained an ET fraction of 57% for the same time period (but with a slightly different definition of ET). Based on the best track records of the Japan Meteorological Agency, the observed ET ratio in the western North Pacific is about 50% (Bieli et al., 2019a), which is close to the ratio in JRA-55, but considerably higher than the fractions obtained from p95 (40%) and the smoothing (35%). In all other basins, however, p95 and the smoothing improve the agreement with JRA-55 compared to the unmodified FLOR-FA parameters. Supporting information Figure S2 shows the effects of p95, sm, and p95 + sm on the ET fractions obtained from JRA-55. Here, p95 only leads to small changes, due to the absence of strong local maxima in the geopotential height fields in the first place. However, the JRA-55 ET fractions are not completely insensitive to p95 since using only a subset (95%) of the geopotential height values within 500-km radius can still give rise to some differences in the diagnosed warm/cold core structure. Applying a smoothing decreases the ET fractions, though to a lesser extent than in FLOR-FA.

In the North Atlantic, p95 has but a marginal effect on the ET fraction. Of all basins, the North Atlantic has the lowest incidence of strong local maxima in the geopotential height fields (supporting information Figure S3), which explains the lower sensitivity to the p95 modification. At this point, we do not understand

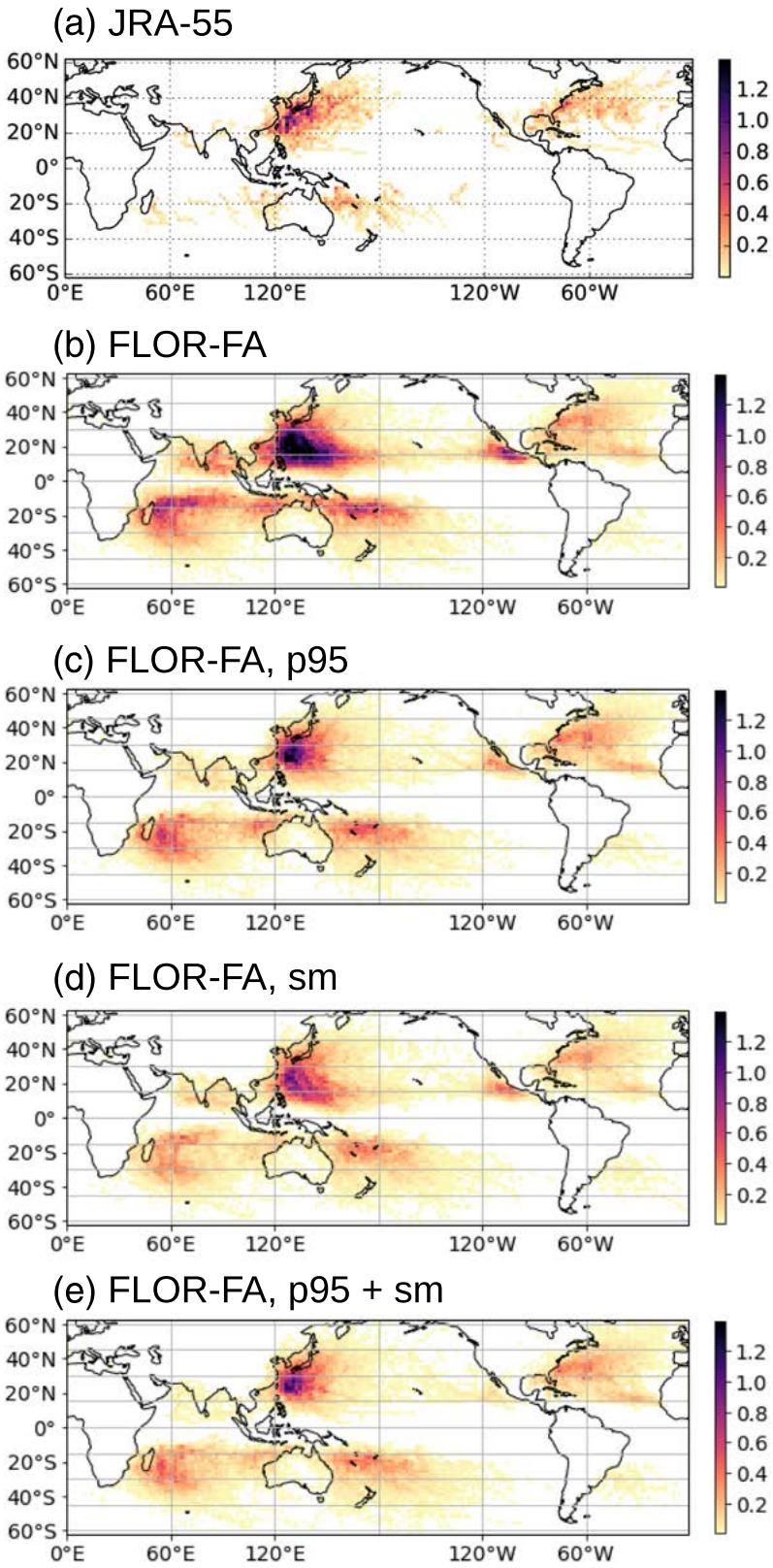

Figure 7. Global ET locations in (a) JRA-55 and (b–e) FLOR-FA (mean of five ensemble members), showing the annual sum of all track points between ET onset and ET completion falling into each 2° × 2° grid box over the time period 1979–2005.

Table 2
Mean Latitude (°N) of ET Onset and ET Completion in JRA-55 and FLOR-FA, in the North Atlantic (NAT), Western North Pacific (WNP), Eastern North Pacific (ENP), North Indian Ocean (NI), South Indian Ocean (SI), Australian Region (AUS), and South Pacific (SP) Basins

	Latitude of ET onset/ET completion						
	NAT	WNP	ENP	NI	SI	AUS	SP
JRA-55	32.2/37.5	29.0/34.7	23.2/25.4	19.5/22.1	−25.2/−28.0	−21.5/−24.3	−21.0/−25.9
FLOR-FA	27.4/35.3	18.4/26.3	14.9/19.6	9.4/12.6	−19.1/−27.3	−15.9/−22.0	−20.3/−25.7
FLOR-FA, p95	29.0/38.1	25.7/32.9	19.6/25.0	12.3/16.2	−23.4/−33.7	−19.9/−28.5	−22.7/−28.6
FLOR-FA, sm	30.4/38.3	24.7/33.0	17.8/24.3	11.2/15.8	−24.4/−33.3	−21.1/−28.9	−23.3/−29.6
FLOR-FA, p95 + sm	29.7/39.1	27.3/35.1	23.7/28.6	14.9/18.3	−24.2/−34.4	−20.6/−29.7	−23.6/−30.3

Note. The time period is 1979–2005, and the FLOR-FA values represent the means of five ensemble members.

why FLOR-FA produces fewer strong grid-scale updrafts in the North Atlantic than in the other basins and whether there is a physical cause for this—for example, an examination of the relationship between storm intensity and the presence of updrafts (not shown) did not hint to any explanations.

Geographical patterns of ET occurrence are shown in Figure 7, as the annual sum of all track points between ET onset and ET completion falling into each 2° × 2° grid box. While ET frequently occurs at unrealistically low latitudes in the unmodified FLOR-FA, p95 and smoothing shift the ET locations poleward into more baroclinic regions. The effect is particularly strong in the western North Pacific, where p95 and smoothing cause northward shifts in the mean latitude of ET onset by 7.3° and 6.3°, respectively (Table 2). There are two possible contributions to these shifts: the northward migration of individual storms' ET locations and the elimination of ET cases altogether such that the distribution of ET locations shifts (but individual storms' ET locations do not). In the western North Pacific, the larger contribution is the shift in individual storms' ET locations: When considering only the ET cases that p95 and the smoothing have in common with the unmodified experiment, the poleward shifts in the mean latitude of ET onset are 4.7° for p95 and 3.8° for the smoothing (not shown). The shift in individual storms' ET caused by p95 and the smoothing is also the dominating effect in most other cases.

In contrast to the effect of lowering the ET fraction, which is stronger for the smoothing than for p95 in all basins (Figure 6), the effect of the two experiments on the ET location depends on the basin—for example, in the North Pacific basins and the North Indian Ocean, p95 shifts ET farther north than the smoothing. ET in FLOR-FA occurs at the highest latitudes when p95 and the smoothing are combined (Table 2 and Figure 7).

The transition time period is defined as the time between the onset and the completion of ET. Table 3 shows the median and lower and upper quartiles of the transition time period in each basin. The median ET duration in FLOR-FA ranges from 36 hr (North Atlantic) to 78 hr (western North Pacific), compared to only 9 hr (eastern North Pacific) to 30 hr (North Atlantic) in JRA-55. The effect of smoothing and p95 depends on the basin, though the combination of the two tends to produce the shortest transition time periods. Like the changes in the ET latitudes, the changes in the transition time periods represent the combined effects of changes in the ET properties of individual storms and changes in the underlying set of ET storms. However, no consistent pattern emerges when evaluating the transition time periods of p95 and those of the smoothing

Table 3
Median and (in Parentheses) Lower and Upper Quartiles of Transition Time Periods (in hr) in JRA-55 and FLOR-FA, in the North Atlantic (NAT), Western North Pacific (WNP), Eastern North Pacific (ENP), North Indian Ocean (NI), South Indian Ocean (SI), Australian Region (AUS), and South Pacific (SP) Basins

	Transition time period (hr)						
	NAT	WNP	ENP	NI	SI	AUS	SP
JRA-55	30 (12, 60)	24 (12, 51)	9 (6, 24)	12 (6, 36)	12 (6, 51)	18 (6, 63)	18 (12, 43)
FLOR-FA	36 (6, 114)	78 (24, 168)	66 (18, 132)	66 (24, 120)	66 (24, 138)	60 (18, 132)	42 (6, 108)
FLOR-FA, p95	42 (6, 120)	30 (12, 102)	36 (12, 131)	42 (12, 102)	66 (24, 126)	54 (18, 140)	30 (6, 102)
FLOR-FA, sm	36 (6, 84)	36 (12, 144)	69 (18, 159)	84 (30, 138)	48 (18, 114)	48 (12, 114)	30 (6, 102)
FLOR-FA, p95 + sm	42 (6, 114)	30 (6, 90)	18 (6, 90)	42 (9, 102)	60 (24, 114)	54 (18, 138)	36 (6, 102)

Note. The time period is 1979–2005, and the FLOR-FA statistics are based on all five ensemble members.

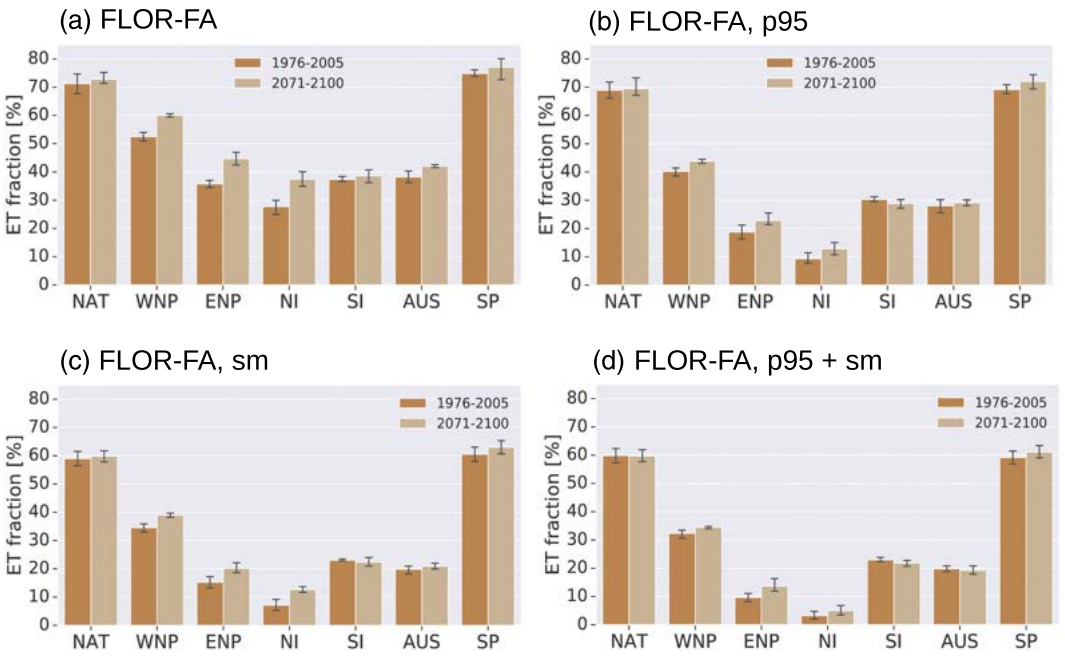

Figure 8. Historical (1976-2005) and future (2071-2100) ET fractions obtained from FLOR-FA. The error bars show the 95% confidence interval estimated from five ensemble members.

on the intersection of their respective sets of ET storms with that of the unmodified experiment—in some basins the difference in the median ET duration increases, and in other basins it decreases. Furthermore, the effect of the combined experiment is not always stronger than that of any individual experiment. An example of this is the South Pacific, where p95 and smoothing each result in a shorter average ET duration than the p95 + sm experiment.

3.3. Projected Changes in ET Activity

Given the sensitivity of the historical ET climatology to the underlying method used to compute the CPS parameters, we explore changes in the future ET activity with an eye to their robustness to these methodological variations. Figure 8 shows the projected changes in global ET fractions between the historical (1976–2005) and future (2071–2100) FLOR-FA simulations, and Table 4 shows the corresponding *p* values of a *t* test on the ensemble mean ET fractions. While the absolute values of the ET fractions vary considerably between the different data sets that result from the four different methods of diagnosing ET as described above, the future trends mostly have the same signs. In most basins, the magnitudes of the changes are small. The increase in the ET fraction in the western North Pacific is the only change that is statistically significant

Table 4
The p Values of a Two-Sided t Test Comparing the Ensemble Mean ET Fraction in the Future (2071–2100) With That in the Historical (1976–2005) Simulation, the Null Hypothesis Being That the Difference Between the Means Is Zero

	ET fractions: *p* values						
	NAT	WNP	ENP	NI	SI	AUS	SP
FLOR-FA	0.536	**<0.001**	**0.001**	**0.002**	0.416	**0.027**	0.373
FLOR-FA, p95	0.841	**0.008**	0.069	0.063	0.202	0.501	0.150
FLOR-FA, sm	0.646	**0.004**	**0.013**	**0.005**	0.472	0.329	0.263
FLOR-FA, p95 + sm	0.931	**0.048**	**0.040**	0.189	0.159	0.645	0.333

Note. Values that are significant at the 0.05 level are shown in boldface. Results are shown for the North Atlantic (NAT), western North Pacific (WNP), eastern North Pacific (ENP), North Indian Ocean (NI), South Indian Ocean (SI), Australian region (AUS), and South Pacific (SP). The ET fractions used to perform the tests are shown in Figure 8.

in all four experiments, although the increases in the eastern North Pacific and the North Indian Ocean are also fairly robust.

The latitude of ET onset is an indicator of the poleward extent of the region that supports tropical development. Figure 9 compares the distributions of the latitude of ET onset in the future and historical time periods. ET begins at the lowest latitudes in the unmodified CPS and at the highest latitudes when p95 and the smoothing are combined (cf. also Table 2). Future changes are generally small, but there is a slight shift toward the equator in most basins. In the western North Pacific and the South Indian Ocean, the changes are significant across all four experiments. However, only in the South Indian Ocean does the latitude of ET completion shift toward lower latitudes as well (not shown).

The equatorward shifting ET locations are contrary to what would be expected from the poleward migration of the average latitude where TCs achieve their lifetime maximum intensity (LMI), which has occurred over the past 30 years in both the Northern and Southern Hemispheres, with the largest contributions coming from the western North Pacific, South Indian Ocean, and South Pacific basins (Kossin et al., 2014). Following the RCP8.5 emission trajectory, an ensemble of Coupled Model Intercomparison Project Phase 5 (CMIP5) models projects the LMI location in the western North Pacific to migrate poleward throughout the 21st century, though the models do not show a significant trend in the historical climate (Kossin et al., 2016). Possible mechanisms that explain the northward shift of the LMI location include the poleward expansion of the region that supports TC development (e.g., Lucas et al., 2014; Studholme & Gulev, 2018), long-term oscillations of sea surface temperatures such as the Pacific Decadal Oscillation or the Atlantic Meridional Mode (e.g., Kossin et al., 2016; Moon et al., 2015; Song & Klotzbach, 2018), or shifts in the TC genesis region (Daloz & Camargo, 2018). In FLOR-FA, there are no significant trends in the time series of LMI locations in the historical or future simulations, nor is there a significant difference between the average LMI location in the future climate and that in the historical climate (not shown). However, the FLOR-FA simulations use the RCP4.5 emission pathway, which imposes a weaker forcing than the RCP8.5 scenario used in Kossin et al. (2016).

Projected changes in the geographical pattern of ET occurrence are shown in Figure 10. The following changes are consistent across the four CPS experiments: In the projected future, more storms undergo ET in the central and eastern North Atlantic and in the western North Pacific (Philippine and East China Sea), and fewer storms undergo ET in the South Indian Ocean.

In the North Atlantic, FLOR-FA projects an increasing number of TCs in the tropical east and in the northeast of the basin, and less frequent TCs in the tropical west of the basin (not shown), which is consistent with the projections of several other climate models (e.g., Bhatia et al., 2018; Colbert et al., 2013; Murakami & Wang, 2010; Zhao & Held, 2012). In FLOR-FA, the increased track density in the east and northeast Atlantic is mostly due to ET storms, since there is no corresponding future increase in the track density of storms that do not undergo ET (not shown). These ET storms typically complete their transitions while recurving to the northeast, and some of them make landfall in western Europe. Haarsma et al. (2013) and Baatsen et al. (2015) found that western Europe will face an enhanced risk of hurricane-force winds and flooding from ET storms in the future. Liu et al. (2017) found similar changes in the Atlantic track patterns and linked them to an increasingly favorable environment for TC development and propagation, which allows TCs to move into the midlatitudes, thereby increasing their probability of undergoing ET.

In the western North Pacific, the ensemble average number of TCs falls from 30 per year during 1976–2005 to 27 during 2071–2100. Despite this decrease in the TC frequency, there is a region of enhanced ET activity, as is to be expected from the higher future ET fraction in that basin (Figure 8). In contrast to the North Atlantic, where the projected increase in ET-related impacts is the result of additional storms reaching western Europe, the increase in the western North Pacific primarily results from TCs undergoing ET in places where they would typically still retain tropical characteristics in the historical time period. The occurrence of more ET events in a region with fewer TCs suggests a change in the environmental conditions and/or properties of the storms passing that region. The projected reduction of ET events in the South Indian Ocean is approximately proportional to the projected reduction of the TC frequency in that basin (not shown).

The future changes in the geographical patterns of ET activity discussed here are the most robust signals across the results from the four CPS algorithms presented in Figure 10. However, none of these changes are statistically significant in a bootstrap hypothesis testing (one test using 10,000 bootstrap replicates for each

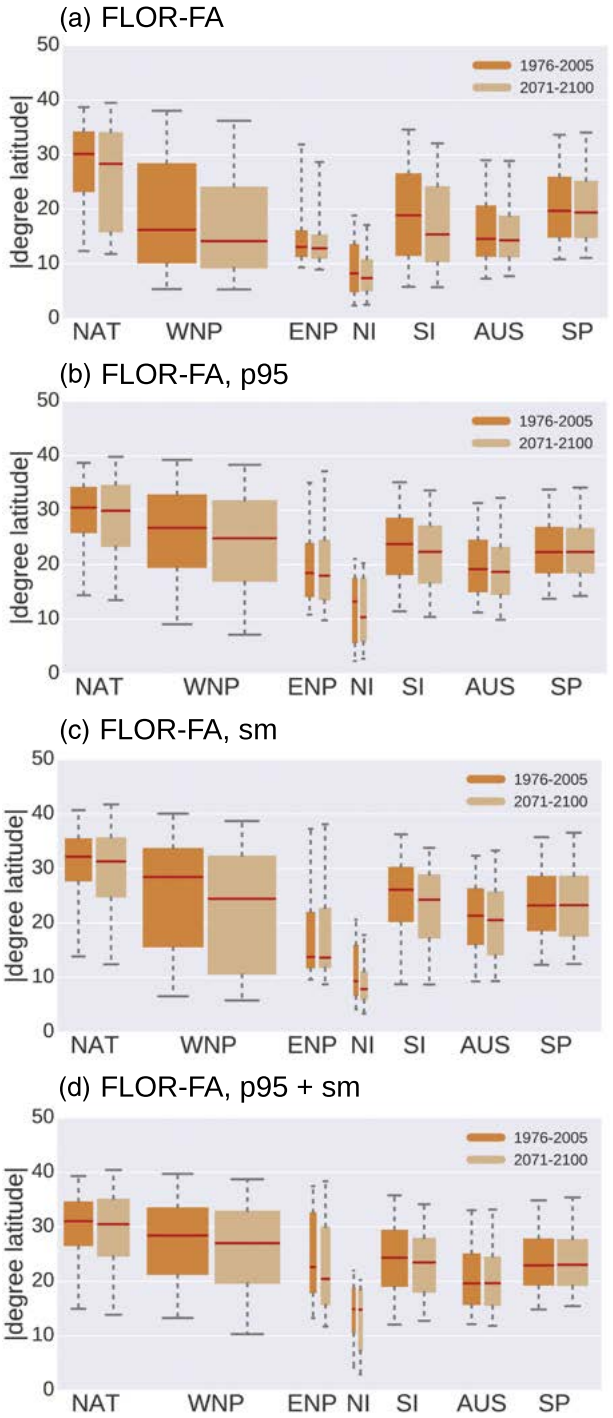

Figure 9. Distribution of the latitude of ET onset based on five historical (1976–2005) and future (2071–2100) FLOR-FA ensemble members, for the North Atlantic (NAT), western North Pacific (WNP), eastern North Pacific (ENP), North Indian Ocean (NI), South Indian Ocean (SI), Australian region (AUS), and South Pacific (SP). The boxes extend from the lower to the upper quartile, with a red line at the median, and the whiskers extend from the 5th to the 95th percentile. The box widths are proportional to the number of ETs in each basin relative to the sum of ETs over all basins.

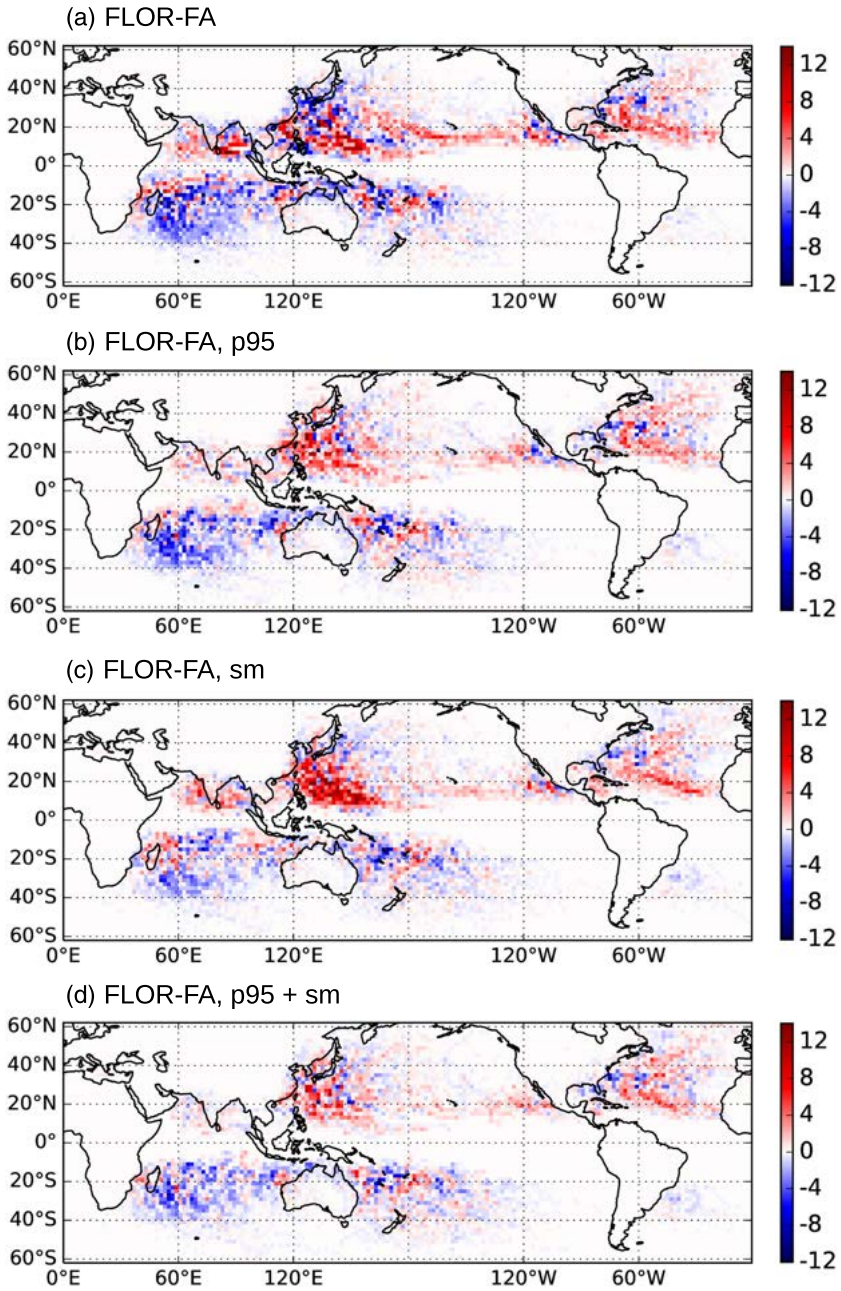

Figure 10. Projected change in ET locations: difference (future – historical) in the ensemble mean of the sum of all track points between ET onset and ET completion over each 30-year time period (2071–2100 and 1976–2005), on a 2° × 2° grid. A red color indicates a future increase in the number of storms undergoing ET in a given grid box, and a blue color indicates a decrease.

2° × 2° grid box). In these multiple hypothesis tests, the method by Wilks (2016) was used to control the false discovery rate at a level of 0.05—the false discovery rate is the expected proportion of false positives, that is, incorrect rejections of the null hypothesis. Controlling the false discovery rate at a level of 0.05 guarantees that the percentage of false positives out of all hypothesis tests is 5% or less.

4. Conclusions

This study examines the ET of TCs in the FLOR-FA climate model, with a focus on how the historical and future statistics of ET occurrence depend on modifications in the algorithm to identify ET in the CPS. The

purpose of the modifications is to address noise in the simulated FLOR-FA fields—specifically, the geopotential height fields contain strong grid-scale convective updrafts, which lead to erroneous diagnoses of the cyclones' warm/cold core structure in the CPS. One of the modifications, a temporal smoothing of the CPS parameters, is a standard procedure that has been applied in a number of studies. The other modification ("p95"), a change in the definition of the thermal wind parameters of the CPS, is new. It removes the sensitivity of the CPS to local maxima in the geopotential height field surrounding the TC.

The smoothing and p95 have somewhat different effects on the probability distributions of the CPS parameters, with p95 resulting in a better agreement with the distributions obtained from the JRA-55 reanalysis. However, the effects of the two modifications on the ET climatology are generally comparable: Both improve the agreement with the observed ET locations, transition time periods, and fractions of TCs undergoing ET.

The strongest signal in the future projections of ET activity is an increased ET fraction in the western North Pacific, which is significant across all four "CPS experiments" (unmodified CPS parameters, p95, smoothing, and p95 combined with the smoothing). The increase in the ET fraction coincides with an equatorward shift (by about 2° latitude in the mean) of the ET onset. This is surprising given the observed poleward shift of the regions that are most favorable for TC development and the associated migration of the average location where TCs achieve their LMI away from the tropics (Kossin et al., 2014). In the western North Pacific, the poleward migration of the LMI location is particularly robust, and it is expected to continue into the future (Kossin et al., 2016). However, FLOR-FA does not simulate any trends in the time series of LMI locations in the historical or future simulations.

We do not know the generality with which the p95 modification introduced in this study will be useful, or how many other models/data sets contain grid-scale structures similar to those in FLOR-FA. However, similar noisy structures have been confirmed in a simulation with the Seamless System for Prediction and EArth System Research (SPEAR, Delworth et al., 2020), the latest modeling system developed at GFDL, in which a new double-plume convection scheme (Zhao et al., 2018) is introduced. It can also be speculated that the Atmosphere Model 2.5 (AM2.5 Delworth et al., 2012) and the High Resolution Atmospheric Model (HiRAM Zhao et al., 2009), which use the same finite volume dynamical core on a cubed-sphere grid (Putman & Lin, 2007) with the same divergence damping coefficient (Zhao & Held, 2012) as FLOR-FA, may be susceptible to localized strong convection akin to that in FLOR-FA. The increasing resolution of climate models and the associated shift from parameterized to resolved convection may also favor grid-scale convective features, and to the extent this is true, examining the applicability of the CPS method to these new data sets and exploring possible modifications will be important contributions to the broader discussion about how to set objective standards for defining ET (McTaggart-Cowan et al., 2018). This study has shown that a percentile-based formulation of the CPS such as p95 may provide a useful alternative in such situations. Another issue that will often arise when attempting to apply the original formulation of the CPS to climate model output is the limited availability of output at multiple vertical levels. This and other issues of the CPS (e.g., the fact that it does not resolve the transitioning cyclone's inner core) have led the research community to recommend a discussion as to whether a universally applicable alternative definition of ET—which would be particularly useful for comparisons between studies on reanalysis data and climate model output—is necessary and achievable (McTaggart-Cowan et al., 2018).

More generally, it seems fairly likely that FLOR-FA is not the only model whose output is different from the data sets that algorithms designed to diagnose aspects of TC structure (including the CPS) were trained on. Issues arising from such differences usually have multiple solutions, and the results of a given study may be sensitive to the choice of that solution. In the example presented here, the changes between future and historical ET activity were overall small and proved relatively insensitive to the choice of p95, the smoothing, or their combination. However, numerous examples of how seemingly small differences in methodologies or parameter values can fundamentally change the outcome of an analysis (e.g., Chattopadhyay et al., 2013; Lo et al., 2016; Seidel et al., 2010; Small et al., 2019; Woollings & Blackburn, 2012) underline the importance of being alert to such problems and careful when applying any diagnostic algorithm to a new model.

Acknowledgments
We thank Yongqiang Sun and Tsung-Lin Hsieh for their thoughtful comments which helped improve the manuscript. M.B. gratefully acknowledges support by the NASA Cooperative Agreement NNX15AJ05A. S. J. C. is partially supported by NOAA's Climate Program Office's Modeling, Analysis, Predictions, and Projections (MAPP) program through grants NA15OAR4310095, NA16OAR4310079, and NA18OAR4310277. A.H.S. also acknowledges funding by NOAA's MAPP Program, through grants NA15OAR4310095 and NA16OAR4310079. G.A.V. is supported by NOAA/OCO (NA18OAR4310418), the Carbon Mitigation Initiative (CMI), and the Cooperative Institute for Modeling the Earth System (CIMES; NA18OAR4320123) at Princeton University. The FLOR-FA tropical cyclone tracks with the "ET flags" (1 if a tropical cyclone undergoes ET, and 0 if it does not) are available on Google drive (at https://drive.google.com/open?id=1fnINJcPI8ApAgnR4qX1U6hsiLuXQpm81).

References

Anber, U. M., Jeevanjee, N., Harris, L. M., & Held, I. M. (2018). Sensitivity of radiative-convection equilibrium to divergence damping in GFDL-FV3-based cloud-resolving model simulations. *Journal of Advances in Modeling Earth Systems*, *10*, 1527–1536. https://doi.org/10.1029/2017MS001225

Baatsen, M., Haarsma, R. J., Van Delden, A. J., & De Vries, H. (2015). Severe autumn storms in future western Europe with a warmer Atlantic ocean. *Climate Dynamics*, *45*, 949–964. https://doi.org/10.1007/s00382-014-2329-8

Bhatia, K., Vecchi, G., Murakami, H., Underwood, S., & Kossin, J. (2018). Projected response of tropical cyclone intensity and intensification in a global climate model. *Journal of Climate*, *31*, 8281–8303. https://doi.org/10.1175/JCLI-D-17-0898.1

Bieli, M., Camargo, S. J., Sobel, A. H., Evans, J. L., & Hall, T. (2019a). A global climatology of extratropical transition. Part I: Characteristics across basins. *Journal of Climate*, *32*, 3557–3582. https://doi.org/10.1175/JCLI-D-17-0518.1

Bieli, M., Camargo, S. J., Sobel, A. H., Evans, J. L., & Hall, T. (2019b). A global climatology of extratropical transition. Part II: Statistical performance of the cyclone phase space. *Journal of Climate*, *32*, 3583–3597. https://doi.org/10.1175/JCLI-D-18-0052.1

Bowyer, P. J., & MacAfee, A. W. (2005). The theory of trapped-fetch waves with tropical cyclones—An operational perspective. *Weather and Forecasting*, *20*, 229–244. https://doi.org/10.1175/WAF849.1

Bromwich, D. H., Fogt, R. L., Hodges, K. I., & Walsh, J. E. (2007). A tropospheric assessment of the ERA-40, NCEP, and JRA-25 global reanalyses in the polar regions. *Journal of Geophysical Research*, *112*, D10111. https://doi.org/10.1029/2006JD007859

Camargo, S. J., & Wing, A. A. (2016). Tropical cyclones in climate models. *Wiley Interdisciplinary Reviews Climate Change*, *7*, 211–237. https://doi.org/10.1002/wcc.373

Chattopadhyay, R., Vintzileos, A., & Zhang, C. (2013). A description of the Madden-Julian oscillation based on a self-organizing map. *Journal of Climate*, *26*, 1716–1732. https://doi.org/10.1175/JCLI-D-12-00123.1

Clarke, L., Edmonds, J., Jacoby, H., Pitcher, H., Reilly, J, & Richels, R. (2007). Scenarios of greenhouse gas emissions and atmospheric concentrations.

Colbert, A. J., Soden, B. J., Vecchi, G. A., & Kirtman, B. P. (2013). The impact of anthropogenic climate change on North Atlantic tropical cyclone tracks. *Journal of Climate*, *26*, 4088–4095. https://doi.org/10.1175/JCLI-D-12-00342.1

Daloz, A. S., & Camargo, S. J. (2018). Is the poleward migration of tropical cyclone maximum intensity associated with a poleward migration of tropical cyclone genesis? *Climate Dynamic*, *50*, 705–715. https://doi.org/10.1007/s00382-017-3636-7

Delworth, T. L., Broccoli, A. J., Rosati, A., Stouffer, R. J., Balaji, V, Beesley, J. A., et al. (2006). GFDL's CM2 global coupled climate models. Part I: Formulation and simulation characteristics. *Journal of Climate*, *19*, 643–674. https://doi.org/10.1175/JCLI3629.1

Delworth, T. L., Cooke, W. F., Adcroft, A., Bushuk, M., Chen, J.-H., Dunne, K. A., et al. (2020). SPEAR—The next generation GFDL modeling system for seasonal to multidecadal prediction and projection. *Journal of Advances in Modeling Earth Systems*, *12*, e2019MS001895. https://doi.org/10.1029/2019MS001895

Delworth, T. L., Rosati, A., Anderson, W., Adcroft, A. J., Balaji, V., Benson, R., et al. (2012). Simulated climate and climate change in the GFDL CM2.5 high-resolution coupled climate model. *Journal of Climate*, *25*, 2755–2781. https://doi.org/10.1175/JCLI-D-11-00316.1

Ebita, A., Kobayashi, S., Ota, Y., Moriya, M., Kumabe, R., Onogi, K., et al. (2011). The Japanese 55-year Reanalysis "JRA-55": An interim report. *SOLA*, *7*, 149–152. https://doi.org/10.2151/sola.2011-038

Evans, J. L., & Hart, R. E. (2003). Objective indicators of the life cycle evolution of extratropical transition for Atlantic tropical cyclones. *Monthly Weather Review*, *131*, 909–925. https://doi.org/10.1175/1520-0493(2003)131h0909:OIOTLCi2.0CO;2

Evans, C., Wood, K. M., Aberson, S. D., Archambault, H. M., Milrad, S. M., Bosart, L. F., et al. (2017). The extratropical transition of tropical cyclones. Part I: Cyclone evolution and direct impacts. *Monthly Weather Review*, *145*, 4317–4344. https://doi.org/10.1175/MWR-D-17-0027.1

Fiorino, M. (2002). Analysis and forecasts of tropical cyclones in the ECMWF 40-year reanalysis (ERA-40). In *Extended Abstract of 25th Conference Hurricanes and Tropical Meteorology* (pp. 261–264).

Haarsma, R. J., Hazeleger, W., Severijns, C., de Vries, H., Sterl, A., Bintanja, R., et al. (2013). More hurricanes to hit western Europe due to global warming. *Geophysical Research Letters*, *40*, 1783–1788. https://doi.org/10.1002/grl.50360

Harris, L. M., Lin, S.-J., & Tu, C. (2016). High-resolution climate simulations using GFDL HiRAM with a stretched global grid. *Journal of Climate*, *29*, 4293–4314. https://doi.org/10.1175/JCLI-D-15-0389.1

Hart, R. E. (2003). A cyclone phase space derived from thermal wind and thermal asymmetry. *Monthly Weather Review*, *131*, 585–616. https://doi.org/10.1175/1520-0493(2003)131h0585:ACPSDFi2.0.CO;2

Hatsushika, H., Tsutsui, J., Fiorino, M., & Onogi, K. (2006). Impact of wind profile retrievals on the analysis of tropical cyclones in the JRA-25 reanalysis. *Journal of the Meteorological Society of Japan Series II*, *84*, 891–905. https://doi.org/10.2151/jmsj.84.891

Jia, L., Yang, X., Vecchi, G. A., Gudgel, R. G., Delworth, T. L., Rosati, A., et al. (2015). Improved seasonal prediction of temperature and precipitation over land in a high-resolution GFDL climate model. *Journal of Climate*, *28*(5), 2044–2062. https://doi.org/10.1175/JCLI-D-14-00112.1

Jones, S. C., Harr, P. A., Abraham, J., Bosart, L. F., Bowyer, P. J., Evans, J. L., et al. (2003). The extratropical transition of tropical cyclones: Forecast challenges, current understanding, and future directions. *Weather and Forecasting*, *18*, 1052–1092. https://doi.org/10.1175/1520-0434(2003)018h1052:TETOTCi2.0.CO;2

Kim, D., Moon, Y., Camargo, S. J., Wing, A. A., Sobel, A. H., Murakami, H., et al. (2018). Process-oriented diagnosis of tropical cyclones in high-resolution GCMs. *Journal of Climate*, *31*(5), 1685–1702. https://doi.org/10.1175/JCLI-D-17-0269.1

Kitabatake, N. (2011). Climatology of extratropical transition of tropical cyclones in the western North Pacific defined by using cyclone phase space. *Journal of the Meteorological Society of Japan. Ser. II*, *89*, 309–325. https://doi.org/10.2151/jmsj.2011-402

Kobayashi, S., Ota, Y., Harada, Y., Ebita, A., Moriya, M., Onoda, H., et al. (2015). The JRA-55 reanalysis: General specifications and basic characteristics. *Journal of the Meteorological Society of Japan. Ser. II*, *93*, 5–48. https://doi.org/10.2151/jmsj.2015-001

Kossin, J. P., Emanuel, K. A., & Camargo, S. J. (2016). Past and projected changes in western North Pacific tropical cyclone exposure. *Journal of Climate*, *29*, 5725–5739. https://doi.org/10.1175/JCLI-D-16-0076.1

Kossin, J. P., Emanuel, K. A., & Vecchi, G. (2014). The poleward migration of the location of tropical cyclone maximum intensity. *Nature*, *509*, 349–52. https://doi.org/10.1038/nature13278

Liu, M., Vecchi, G. A., Smith, J. A., & Murakami, H. (2017). The present-day simulation and twenty-first-century projection of the climatology of extratropical transition in the North Atlantic. *Journal of Climate*, *30*, 2739–2756. https://doi.org/10.1175/JCLI-D-16-0352.1

Liu, M., Vecchi, G. A., Smith, J. A., & Murakami, H. (2018). Projection of landfalling-tropical cyclone rainfall in the eastern United States under anthropogenic warming. *Journal of Climate*, *31*, 7269–7286. https://doi.org/10.1175/JCLI-D-17-0747.1

Liu, M., Vecchi, G. A., Smith, J. A., Murakami, H., Gudgel, R., & Yang, X. (2018). Towards dynamical seasonal forecast of extratropical transition in the North Atlantic. *Geophysical Research Letters*, *45*, 12,602–12,609. https://doi.org/10.1029/2018GL079451

Lo, Y. E., Charlton-Perez, A. J., Lott, F. C., & Highwood, E. J. (2016). Detecting sulphate aerosol geoengineering with different methods. *Science Report*, *6*, 39,169. https://doi.org/10.1038/srep39169

Loridan, T., Khare, S., Scherer, E., Dixon, M., & Bellone, E. (2015). Parametric modeling of transitioning cyclone wind fields for risk assessment studies in the western North Pacific. *Journal of Applied Meteorology and Climatology*, *54*, 624–642. https://doi.org/10.1175/JAMC-D-14-0095.1

Loridan, T, Scherer, E, Dixon, M, Bellone, E, & Khare, S (2014). Cyclone wind field asymmetries during extratropical transition in the western North Pacific. *Journal of Applied Meteorology and Climatology*, *53*, 421–428. https://doi.org/10.1175/JAMC-D-13-0257.1

Lucas, C., Timbal, B., & Nguyen, H. (2014). The expanding tropics: A critical assessment of the observational and modeling studies. *Wiley Interdisciplinary Reviews: Climate Change*, *5*, 89–112. https://doi.org/10.1002/wcc.251

Matyas, C. J. (2013). Processes influencing rain-field growth and decay after tropical cyclone landfall in the United States. *Journal of Applied Meteorology and Climatology*, *52*, 1085–1096. https://doi.org/10.1175/JAMC-D-12-0153.1

McTaggart-Cowan, R., Evans, C., Aberson, S., Archambault, H., Bosart, L., Camargo, S., et al. (2018). WMO/TCP/WWW Report of the Ninth International Workshop on Tropical Cyclones (IWTC-9). Subtopic 4.3. Extratropical transition. http://www.wmo.int/pages/prog//arep/wwrp/tmr/documents/IWTC-9_Subtopic_4-3.pdf

Moon, I.-J., Kim, S.-H., Klotzbach, P., & Chan, J. C. (2015). Roles of interbasin frequency changes in the poleward shifts of the maximum intensity location of tropical cyclones. *Environmental Research Letters*, *10*, 104004. https://doi.org/10.1088/1748-9326/10/10/104004

Moorthi, S., & Suarez, M. J. (1992). Relaxed Arakawa-Schubert. A parameterization of moist convection for General Circulation Models. *Monthly Weather Review*, *120*, 978–1002. https://doi.org/10.1175/1520-0493(1992)120h0978:RASAPOi2.0.CO;2

Murakami, H. (2014). Tropical cyclones in reanalysis data sets. *Geophysical Research Letters*, *41*, 2133–2141. https://doi.org/10.1002/2014GL059519

Murakami, H., Vecchi, G. A., Delworth, T. L., Paffendorf, K., Jia, L., Gudgel, R., & Zeng, F. (2015). Investigating the influence of anthropogenic forcing and natural variability on the 2014 Hawaiian hurricane season. *Bulletin of the American Meteorological Society*, *96*, S115–S119. https://doi.org/10.1175/BAMS-D-15-00119.1

Murakami, H., Vecchi, G. A., Delworth, T. L., Wittenberg, A. T., Underwood, S., Gudgel, R., et al. (2017). Dominant role of subtropical Pacific warming in extreme eastern Pacific hurricane seasons: 2015 and the future. *Journal of Climate*, *30*, 243–264. https://doi.org/10.1175/JCLI-D-16-0424.1

Murakami, H., Vecchi, G. A., Underwood, S., Delworth, T. L., Wittenberg, A. T., Anderson, W. G., et al. (2015). Simulation and prediction of category 4 and 5 hurricanes in the high-resolution GFDL HiFLOR coupled climate model. *Journal of Climate*, *28*, 9058–9079. https://doi.org/10.1175/JCLI-D-15-0216.1

Murakami, H., Vecchi, G. A., Villarini, G., Delworth, T. L., Gudgel, R., Underwood, S., et al. (2016). Seasonal forecasts of major hurricanes and landfalling tropical cyclones using a high-resolution GFDL coupled climate model. *Journal of Climate*, *29*, 7977–7989. https://doi.org/10.1175/JCLI-D-16-0233.1

Murakami, H., Villarini, G., Vecchi, G. A., Zhang, W., & Gudgel, R. (2016). Statistical-dynamical seasonal forecast of North Atlantic and U.S. landfalling tropical cyclones using the high-resolution GFDL FLOR coupled model. *Monthly Weather Review*, *144*, 2101–2123. https://doi.org/10.1175/MWR-D-15-0308.1

Murakami, H., & Wang, B. (2010). Future change of North Atlantic tropical cyclone tracks: Projection by a 20-km-mesh global atmospheric model. *Journal of Climate*, *23*, 2699–2721. https://doi.org/10.1175/2010JCLI3338.1

Putman, W. M., & Lin, S.-J. (2007). Finite-volume transport on various cubed-sphere grids. *Journal of Computational Physics*, *227*, 55–78. https://doi.org/10.1016/j.jcp.2007.07.022

Seidel, D. J., Ao, C. O., & Li, K. (2010). Estimating climatological planetary boundary layer heights from radiosonde observations: Comparison of methods and uncertainty analysis. *Journal of Geophysical Research*, *115*, D16113. https://doi.org/10.1029/2009JD013680

Small, R. J., Msadek, R., Kwon, Y.-O., Booth, J. F., & Zarzycki, C. (2019). Atmosphere surface storm track response to resolved ocean mesoscale in two sets of global climate model experiments. *Climate Dynamic*, *52*, 2067–2089. https://doi.org/10.1007/s00382-018-4237-9

Song, J., & Klotzbach, P. J. (2018). What has controlled the poleward migration of annual averaged location of tropical cyclone lifetime maximum intensity over the western North Pacific since 1961? *Geophysical Research Letters*, *45*, 1148–1156. https://doi.org/10.1002/2017GL076883

Stocker, T. F., Qin, D., Plattner, G.-K., Alexander, L. V., Allen, S. K., Bindoff, N. L., et al. (2013). Technical summary. In T. F. Stocker, D. Qin, G.-K. Plattner, M. Tignor, S. K. Allen, et al. (Eds.), *Climate change 2013: The physical science basis. Contribution of Working Group I to the Fifth Assessment Report of the Intergovernmental Panel on Climate Change* (pp. 33–155). Cambridge, United Kingdom and New York, NY, USA: Cambridge University Press. www.climatechange2013.org

Studholme, J., & Gulev, S. (2018). Concurrent changes to Hadley circulation and the meridional distribution of tropical cyclones. *Journal of Climate*, *31*, 4367–4389. https://doi.org/10.1175/JCLI-D-17-0852.1

Thomson, A. M., Calvin, K. V., Smith, S. J., Kyle, G. P., Volke, A., Patel, P., et al. (2011). RCP4.5: A pathway for stabilization of radiative forcing by 2100. *Climate Change*, *109*, 77. https://doi.org/10.1007/s10584-011-0151-4

Vecchi, G. A., Delworth, T, Gudgel, R., Kapnick, S, Rosati, A., Wittenberg, A. T., et al. (2014). On the seasonal forecasting of regional tropical cyclone activity. *Journal of Climate*, *27*, 7994–8016. https://doi.org/10.1175/JCLI-D-14-00158.1

Walsh, K. J. E., Fiorino, M., Landsea, C. W., & McInnes, K. L. (2007). Objectively determined resolution-dependent threshold criteria for the detection of tropical cyclones in climate models and reanalyses. *Journal of Climate*, *20*, 2307–2314. https://doi.org/10.1175/JCLI4074.1

Wilks, D. S. (2016). "The stippling shows statistically significant grid points": How research results are routinely overstated and overinterpreted, and what to do about it. *Bulletin of the American Meteorological Society*, *97*, 2263–2273. https://doi.org/10.1175/BAMS-D-15-00267.1

Wood, K. M., & Ritchie, E. A. (2014). A 40-year climatology of extratropical transition in the eastern North Pacific. *Journal of Climate*, *27*, 5999–6015. https://doi.org/10.1175/JCLI-D-13-00645.1

Woollings, T., & Blackburn, M. (2012). The North Atlantic jet stream under climate change and its relation to the NAO and EA patterns. *Journal of Climate*, *25*, 886–902. https://doi.org/10.1175/JCLI-D-11-00087.1

Yang, X., Vecchi, G. A., Gudgel, R. G., Delworth, T. L., Zhang, S., Rosati, A., et al. (2015). Seasonal predictability of extratropical storm tracks in GFDL's high-resolution climate prediction model. *Journal of Climate*, *28*, 3592–3611. https://doi.org/10.1175/JCLI-D-14-00517.1

Zarzycki, C. M., Thatcher, D. R., & Jablonowski, C. (2017). Objective tropical cyclone extratropical transition detection in high-resolution reanalysis and climate model data. *Journal of Advances in Modeling Earth Systems*, *9*, 130–148. https://doi.org/10.1002/2016MS000775

Zhang, W., Vecchi, G. A., Murakami, H., Villarini, G., & Jia, L. (2016). The Pacific meridional mode and the occurrence of tropical cyclones in the western North Pacific. *Journal of Climate*, *29*, 381–398. https://doi.org/10.1175/JCLI-D-15-0282.1

Zhang, W., Vecchi, G. A., Villarini, G., Murakami, H., Rosati, A., Yang, X., et al. (2017). Modulation of western North Pacific tropical cyclone activity by the Atlantic Meridional Mode. *Climate Dynamics*, *48*, 631–647. https://doi.org/10.1175/JCLI-D-12-00210.1

Zhao, M., Golaz, J.-C., Held, I. M., Guo, H., Balaji, V., Benson, R., et al. (2018). The GFDL global atmosphere and land model AM4.0/LM4.0: 2. Model description, sensitivity studies, and tuning strategies. *Journal of Advances in Modeling Earth Systems*, *10*, 735–769. https://doi.org/10.1002/2017MS001209

Zhao, M., & Held, I. M. (2012). TC-permitting GCM simulations of hurricane frequency response to sea surface temperature anomalies projected for the late-twenty-first century. *Journal of Climate*, *25*(8), 2995–3009. https://doi.org/10.1175/JCLI-D-11-00313.1

Zhao, M., Held, I. M., Lin, S.-J., & Vecchi, G. A. (2009). Simulations of global hurricane climatology, interannual variability, and response to global warming using a 50-km resolution GCM. *Journal of Climate*, *22*, 6653–6678. https://doi.org/10.1175/2009JCLI3049.1